JOURNAL OF MATERIALS SCIENCE 25 (1990) 1219–1230

Microstructural characterization of rapidly solidified nickel-base superalloys

SANG-YUL LEE*, PHILIP NASH
Department of Metallurgical and Materials Engineering, Illinois Institute of Technology, Chicago, Illinois 60616, USA

S. BRADLEY
UOP Research Center, P.O. Box 5016, Des Plaines, Illinois 60017, USA

Several Ni–Al–Mo-based eutectic superalloys were rapidly solidified using a chilled block melt spinning process. The effects of rapid solidification on the microstructure were studied using optical microscopy, transmission electron microscopy (TEM), and scanning transmission electron microscopy (STEM). Results showed, except for the alloy containing chromium, that the microstructure varied as a function of ribbon thickness from segregationless solidification at the wheel side of the ribbon to dendritic solidification at the free side. In addition, alloys with the same solidification rate showed a large variation in microstructure depending upon the solid state cooling rate. The rapidly solidified eutectic Ni–Al–Mo alloy with a small amount of rhenium and vanadium did not show any improvement on delaying or prohibiting the formation of the embrittling δ-NiMo phase on ageing at 1000° C. This was determined from microstructural as well as chemical analysis using STEM. Differential thermal analysis was used to obtain melting temperature, γ'-Ni_3Al solvus, and heat of formation for the alloys.

1. Introduction

Rapid solidification processes (RSP) were practiced industrially over 150 years ago in the production of lead pallets [1]. It was however not until about a quarter of a century ago that the metallurgical advantages of RSP such as increased degrees of homogeneity, higher levels of supersaturation, refined grain size, and novel microstructures, including metallic glass were first recognized from the work of Duwez and his associates on splat quenching from the molten state [2–4]. Since then numerous studies have been made in the area of RSP and many reports on rapidly solidified materials with superior engineering properties such as better corrosion resistance and high temperature mechanical properties, have been published.

The chilled block melt spinning (CBMS) process is one of many processes in the category of RSP and has been used for both research sample preparation for alloys of aluminium, iron, nickel, copper, lead, and many others, and commercial production at high rate (about 60 ft sec^{-1}) for iron- and nickel-base alloys [5, 6]. By this process technique uniquely shaped products, such as tool steel ribbon, can be made without rolling and annealing treatments [5]. Compared with products from other rapid solidification processes, the continuous ribbon product of the CBMS process is more convenient to manipulate for further studies. In addition, the high cooling rates associated with the fast solid state cooling in this process make it possible for the alloy to achieve complete solid solubility in the as-cast condition. This means that it is possible to study the characteristics of alloy phase transformations (especially the very early stages) without solution treatment before ageing.

In an attempt to develop Ni-base superalloys for high temperature structural applications both directional solidification [7–15] and rapid solidification processing [16–23] have been used extensively. Directionally solidified eutectic Ni-base superalloys have received considerable interest in the past decade as candidates for a new family of turbine-blade materials. In particular, among the many alloy systems investigated a directionally solidified eutectic Ni–Al–Mo system [7–12] has been proven to be one of the more promising alloys as an advanced gas turbine blade material since its ductile/ductile composite structure is reported to yield about 55° C operating temperature improvement over the current best superalloy used in aeroengines [24]. This composite structure showed further improvement in room temperature mechanical properties through modification of the γ'-Ni_3Al morphology from massive to particular through a post-solidification heat treatment [7, 25]. However, the stability of the composite with the modified microstructure is reported to deteriorate at high temperatures, resulting from the formation of a brittle intermetallic compound, δ-NiMo through a pseudo-peritectoid reaction [10, 26, 27]. This phase reduces the high temperature properties, such as creep–rupture strength. However, no attempts to avoid or delay the formation of this intermetallic phase have been reported in the literature to date.

Present address: Metalock Corporation, 205 Willow Springs Road, Willow Springs, Illinois 60480, USA.

0022–2461/90 $03.00 + .12

The objective of this work was to determine the effects of rapid solidification and alloying on the microstructure of Ni–Al–Mo base alloys. In particular, the stability of the δ-NiMo intermetallic compound was investigated. Extensive studies of the as-cast ribbon were used as a base for subsequent studies on phase transformations, on alloying effects on the formation of intermetallic compounds, and on property–microstructure relationships, which are reported elsewhere [28].

2. Experimental procedure

In this work, a Ni–Al–Mo ternary eutectic alloy was used as a base with small alloying additions being made to the alloy. The compositions listed in Table I, were produced by melting the component elements with over 99.9% purity in a vacuum induction furnace to produce 200 g ingots. During melting the vacuum was maintained at 1.2×10^{-4} Pa. The molten metal held in an alumina crucible was poured into a copper mould to produce a $0.5 \times 0.5 \times 5$ in alloy bar. The bar was weighed and the weight loss was determined to be negligible. The bar was cut into approximately 25 g pieces for the melt spinning process.

Approximately 25 g of alloy was put into a dense alumina crucible and heated to 1400° C and held for 2 min. The molten metal was then pressurized to 12.5 p.s.i. using helium gas to cause ejection through a 0.04 inch diameter nozzle onto a rotating 4340 steel wheel with a diameter of 7 in. Two different wheel speeds, yielding 20 and 30 m sec^{-1} surface speeds, were used to study the effect of the wheel speed on the cooling rates and the microstructure.

The mechanically polished samples for optical microscopic studies wre etched using Marble's reagent. The thickness of the ribbon was measured by photographing the cross section of the ribbon.

In order to study the surface morphologies of both sides of the ribbon, carbon replicas of the ribbon surfaces were produced. The samples were electrolytically etched in 2% citric acid plus 2% ammonium sulphate in distilled water for 30 sec at an applied voltage of 3–5 V.

For the TEM and STEM studies, 3 mm discs were cut from the as-cast ribbons and electropolished. The electrolyte used for this study consisted of one part (by volume) of 70% perchloric acid and 9 parts of high purity methanol and the temperature of the electrolyte was maintained at -60° C. In order to study the microstructure of ribbon as a function of the ribbon thickness a single side polishing technique was used [29]. Samples were examined in a JEOL 100 CX at 100 kV and a Phillips 400EM at 120 kV. A vacuum generators VG-5 dedicated STEM with an operating voltage of 100 kV was used for the STEM study. Heat treatments at 1000° C for MS20 samples were performed using a vacuum furnace connected to a diffusion pump and samples were furnace-cooled.

Differential thermal analysis (DTA) was carried out using either a Perkin-Elmer (model DSCII) differential scanning calorimeter (DSC) or a Netzsch DTA. The DSC instrument was calibrated using the melting of gold. Samples of about 50 mg were heated at 20° C min^{-1} up to 1450° C and cooled at the same rate.

TABLE I Alloy compositions

Alloy designation	Composition (at %)						Wheel speed (m sec^{-1})
	Ni	Al	Mo	V	Re	Cr	
MS20	65	13.5	19.2	1.9	0.4	–	20
MS30	65	13.5	19.2	1.9	0.4	–	30
MS30E	65.7	17.6	16.7	–	–	–	30
MS30Cr	68	12	10	–	–	10	30

3. Results and discussion

3.1. Differential thermal analysis

The DSC and DTA results are shown in Fig. 1. The information obtained from these experiments is summarized in Table II. The melting temperature and the γ' solvus of MS30 show close agreement between the results obtained from the two different instruments used, considering that the Perkin-Elmer gives about a 10° C temperature error in the melting point of pure gold [30] as shown in Table II. From the results obtained using the Netzsch DTA, the melting point of MS30 is in the range from 1302° C on heating to 1297° C on cooling. Since the alloy is expected to undercool during cooling, especially with the high cooling rate (20° C min^{-1}) used in this study, the transformation temperature on heating was taken to be more accurate. The value of the γ' solvus of MS30 was determined to be 1260° C in this study, although no clear peak is produced for this transformation so that there is some uncertainty in this value. The DTA on MS20 which has the same composition as MS30 but spun at a different wheel speed gave similar results for the melting temperature of the alloy. Knowing the heat of fusion of the reference pure gold, the heat of fusion for MS30 was calculated to be 8.9 ± 0.5 kJ mol^{-1}.

The melting temperature of MS30E was measured to be 1290° C on heating and 1289° C on cooling. This is about 10–15° C lower than the results on the melting temperature of the eutectic Ni–Al–Mo alloy reported by Pearson and Lemkey (1300° C [31]) and Wakashima *et al.* (1305° C [26]). The melting temperature of MS30Cr was measured to be 1324° C on heating and 1316° C on cooling. Hence the chromium containing alloy has the highest melting temperature and the

TABLE II Results of differential thermal analysis

	Perkin-Elmer†			Netzsch		
	Alloy			Alloy		
	MS30	MS20	Au*	MS30	MS30E	MS30Cr
Liquidus/solidus onset temperature (° C)						
Heating	1291	1290	1054	1302	1290	1324
Cooling	1283	1285	1045	1297	1289	1316
γ' solvus (° C)						
Heating	1251	1249		1260		
Cooling	1218	1214		1225		
Heat of fusion (kJ mol^{-1})						
Heating	9.369					
Cooling	8.472					

*Used as a reference for temperature and enthalpy calibration.
†Equipment used.

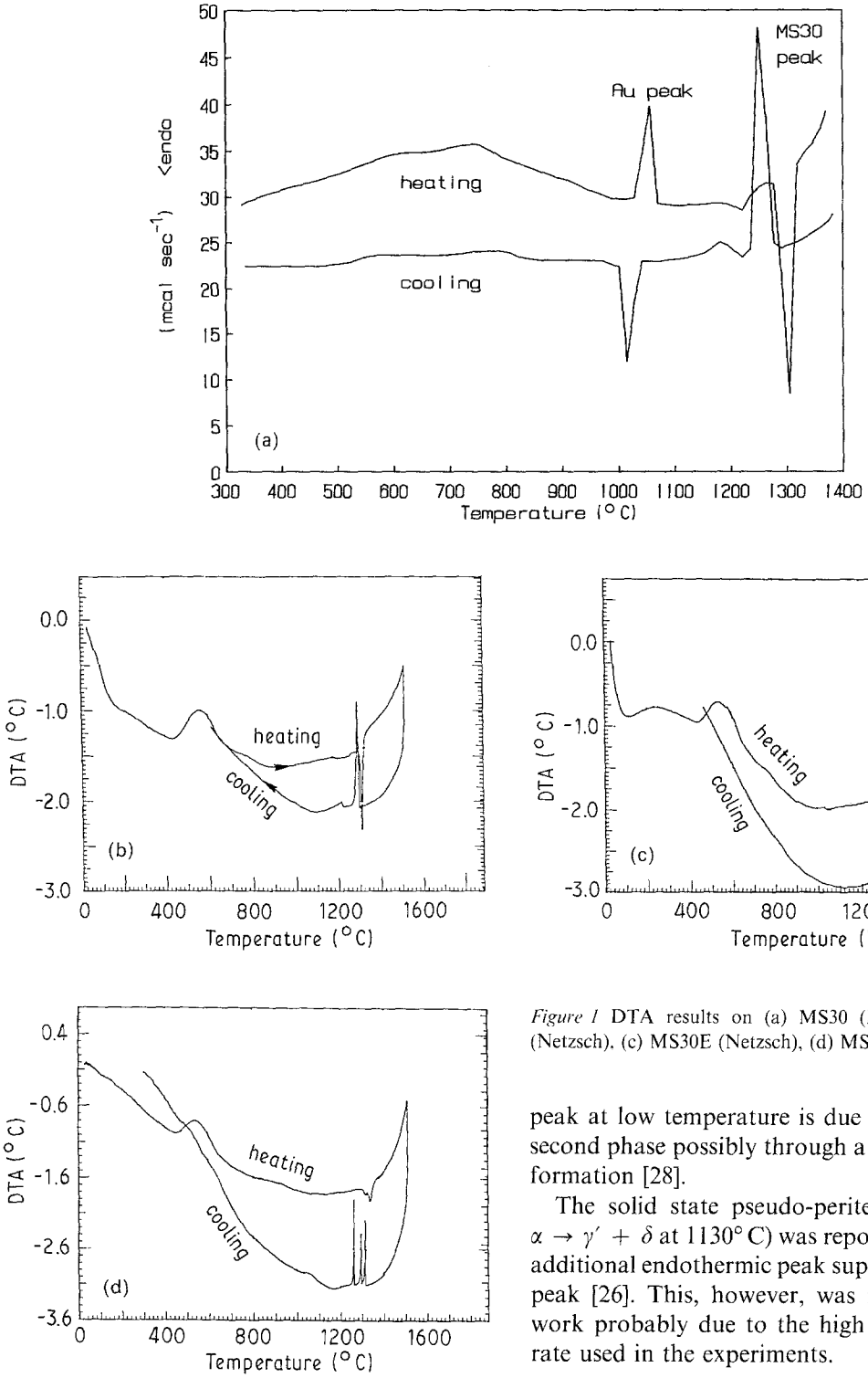

Figure 1 DTA results on (a) MS30 (Perkin-Elmer), (b) MS30 (Netzsch), (c) MS30E (Netzsch), (d) MS30Cr (Netzsch).

eutectic MS30E the lowest. The DTA curves for MS30E and MS30Cr are shown in Fig. 1c and d, respectively.

At around 600° C a shallow, broad peak was observed consistently in all four specimens. This peak is believed to be due to complex solid state reactions including metastable transformations. Even though detailed analysis on this peak was not attempted, it can be deduced from the exothermic nature of the peak on heating MS30 in Figs 1a and b that the rapidly solidified alloy transforms from its as-cast metastable state to an equilibrium state with lower free energy. This involves spinodal ordering and precipitation of α-Mo as well as metastable precipitates [28]. On cooling MS30, Figs 1a and b, the exothermic peak at low temperature is due to precipitation of a second phase possibly through a discontinuous transformation [28].

The solid state pseudo-peritectoid reaction ($\gamma + \alpha \rightarrow \gamma' + \delta$ at 1130° C) was reported to give rise to an additional endothermic peak superimposed with the γ' peak [26]. This, however, was not observed in this work probably due to the high heating and cooling rate used in the experiments.

3.2. Optical metallography

Optical micrographs showing the structural developments through the thickness of the as-cast ribbons of MS20, MS30, MS30Cr and MS30E are shown in Figs 2a to d. The side which contacted the wheel will be referred to as the wheel side (WS) and the opposite side will be called the free side (FS), as indicated in Fig. 2. The casting direction is indicated by arrows. The local thickness of the ribbon shows some variation due to variability in the many processing parameters, such as wheel surface roughness, melt flowability, and liquid metal wettability. In general the ribbon melt-spun at low wheel speed has a consistently larger thickness than that produced using a higher wheel speed. The average thickness of MS20 is about $45 \pm 5\,\mu m$ and the alloys melt-spun at $30\,m\,sec^{-1}$

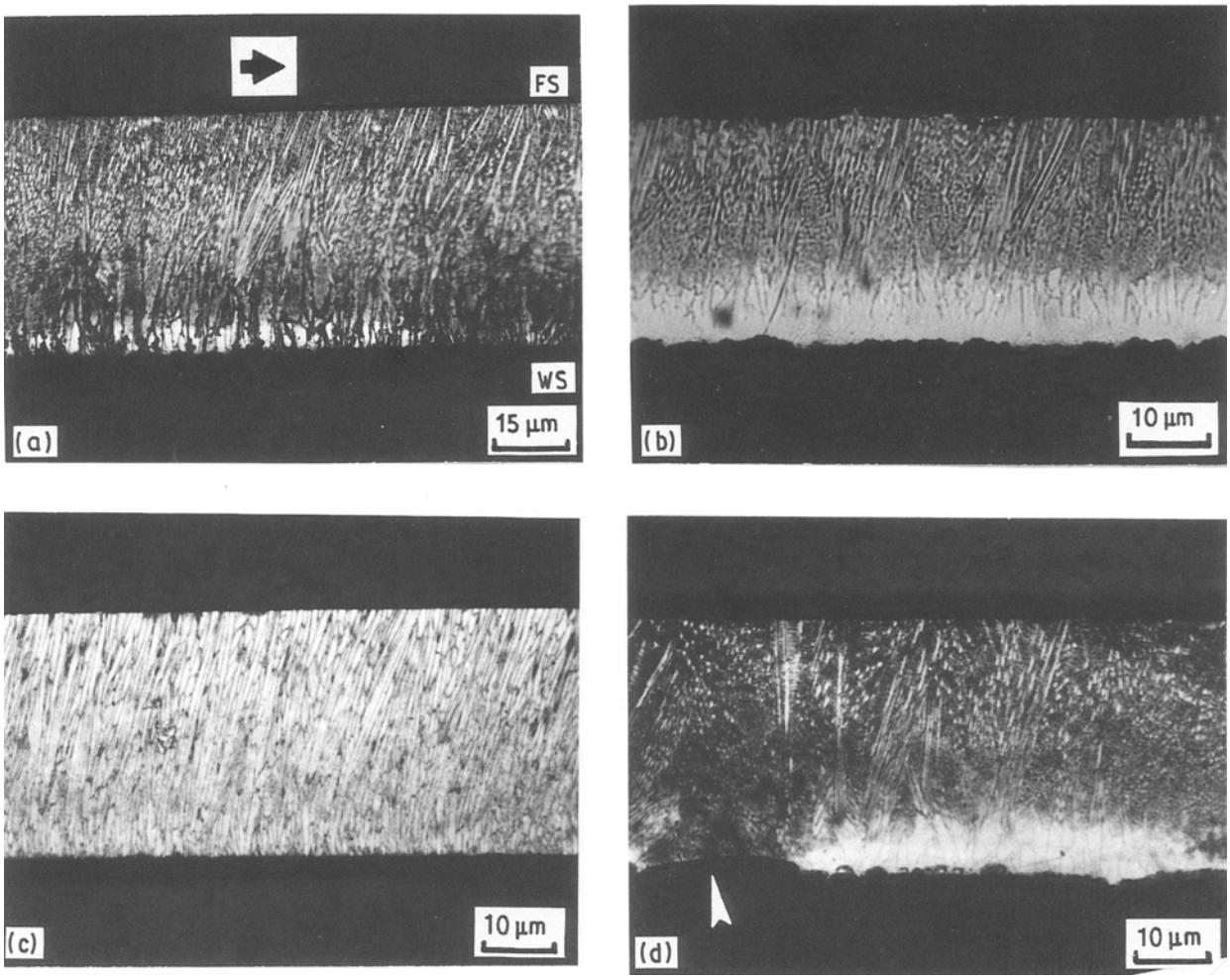

Figure 2 Optical micrographs showing the transverse section of the ribbon, (a) MS20, (b) MS30, (c) MS30Cr, (d) MS30E.

have an average thickness of 30 ± 3 μm independent of the alloy composition. The width of the ribbon was independent of the wheel speed used and the compositions and was measured to be 3.5 ± 0.5 mm.

The structural developments from the wheel side to the free side of the ribbon were different depending upon the composition. With the exception of MS30Cr, the alloys underwent planar solidification followed by cellular solidification as the solidification front traversed from the wheel side to the free side of the ribbon. A transition region between two solidification modes was observed and dendritic solidification was observed on the free surface of the ribbon. The average width of the planar solidification region was about 6 μm and independent of the wheel speed. A recent study [32] has shown that the solidification rate varies as a function of thickness. Based on melt puddle resident time measurements, Huang *et al.* [33] reported the relationship between ribbon thickness and the solid–liquid interface growth velocity in a melt-spun Ni-base superalloy. According to this relationship, the growth velocity in the planar solidification region is higher than 608.3 mm sec^{-1} and the growth velocities in the cellular solidification region are greater than 81.1 and 121.7 mm sec^{-1} for ribbons cast at 20 and 30 m sec^{-1}, respectively. MS30Cr exhibits cellular solidification exclusively throughout the ribbon, Fig. 2c. The columnar grains in the cellular solidification region lean toward the leading end of the ribbon at varying angles from about 10 to 25°, depending upon the location, compositions, and casting speeds. Similar observations have been reported in previous investigations of melt-spun Ni–Mo [34] and Ni-base superalloys [35–37]. Even though the quantitative relationship between the inclination degree and variables, such as composition and casting speed are not elucidated to date, the effect is probably due to solute rejection at the solid–liquid interface. The work by Tewari and Glasgow [34] on melt-spun Ni–Mo alloys supports this suggestion, in that by applying higher wheel speed (higher cooling rate) the solute rejection at the interface was restricted resulting in planar solidification. It is also noted that the width of the cells in the cellular solidification region increases on going from the wheel side to free side, implying a decreasing solidification rate toward the free side of the ribbon.

Occasionally, a different solidification morphology through the ribbon was observed as shown in Fig. 2d. This occurs when the molten metal does not contact the substrate wheel surface. In this region (indicated by the arrow) the planar solidification region was missing and the somewhat different solidification morphology resulted from the change in the heat transfer direction.

The change in the solidification morphologies within the ribbon can be understood using the relationship between temperature gradient and interface velocity

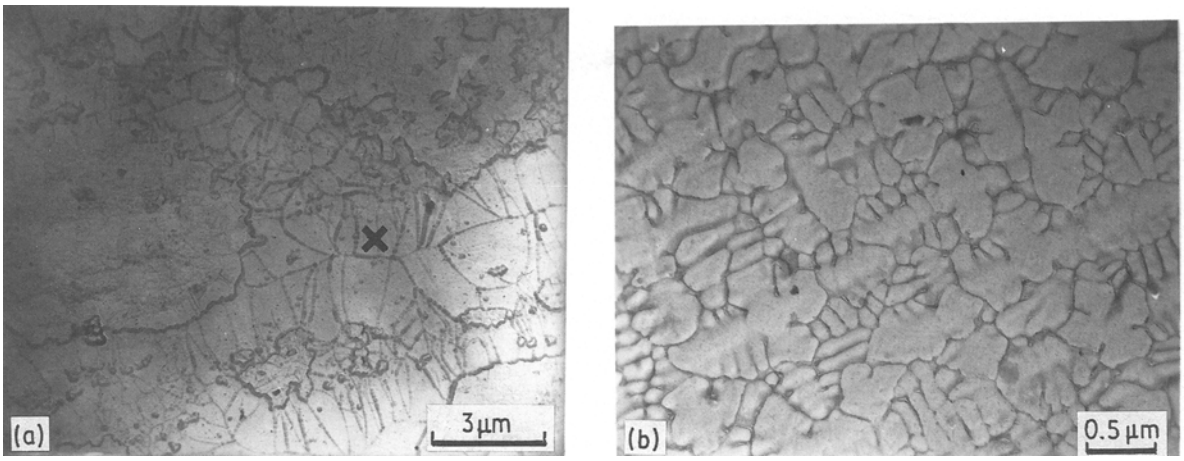

Figure 3 Carbon replicas of surface morphologies of the melt-spun ribbon, (a) wheel side, (b) free side.

[38]. At the beginning of solidification there is a large temperature gradient in the superheated melt and this results in planar solidification near the wheel side of the ribbon. On further solidification, the temperature gradient decreases and the protuberances on the planar front begin to form in random directions, resulting in a transition region in the ribbon. The protuberances with a favoured solidification direction (⟨100⟩ in fcc alloys) continue growing to form the cellular morphology, while others decay. A transition from cellular solidification to dendritic was not observed optically in the alloys studied in this work.

3.3. TEM microstructures of as-cast alloys

3.3.1. MS20 alloy

Surface morphologies of the as-cast ribbon were examined using the carbon replica technique. The surface morphologies of the wheel side and the free side of the ribbon are shown in Figs 3a and b, respectively. Figure 3a shows two different areas: contacted and noncontacted. The large featureless area represents a region where the ejected molten metal contacted the wheel surface and the other is the noncontacted area. The observation of two different areas in the surface morphology of the wheel side of the ribbon is consistent with the transverse optical micrograph in Fig. 2d. The solidification morphology at the noncontacted area (marked X in Fig. 3a) suggests that heat transfer occurs towards the contacting areas. The featureless area in Fig. 3a represents the surface morphology of the region where planar solidification is observed in Fig. 2d. Dendritic solidification is observed at the free side of the ribbon, as shown in Fig. 3b. The secondary dendrite arm spacing was measured to be on the order of 0.1 μm. The equivalent cooling rate with this value is about 10^5–10^6 K sec^{-1} using the empirical relationship between the secondary dendrite arm spacing and the solidification rate for Inconel 718 [35].

Preferential electropolishing was performed in order to investigate the microstructure as a function of ribbon thickness. No apparent sign of transformation in the planar solidification region is observed, Fig. 4a. The grains in the planar solidification region are polygonal, sharply-edged, and average grain size is 0.7 μm. Assuming every grain represents a single nucleation event [33], the nucleation density is about 2×10^{16} mm^{-1}. In the transition region between the planar and the cellular solidification region, development of the cell structure is observed as well as the trace of a second phase at the boundaries, Fig. 4b. The average grain size and the average cell size in the transition region are on the order of 0.8 and 0.15 μm,

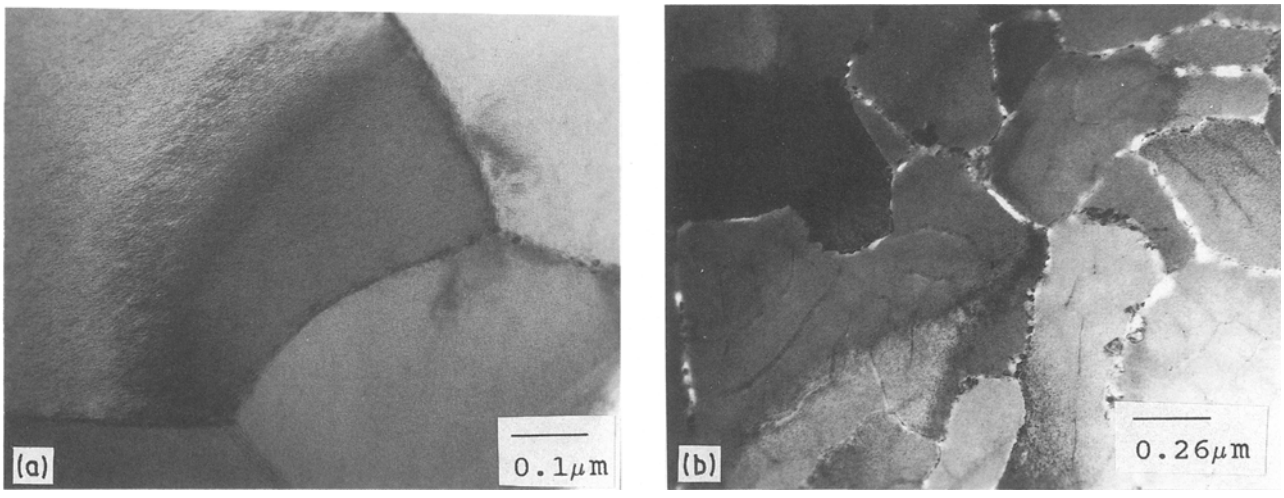

Figure 4 TEM micrographs of MS20 from (a) planar solidification region, (b) transition region.

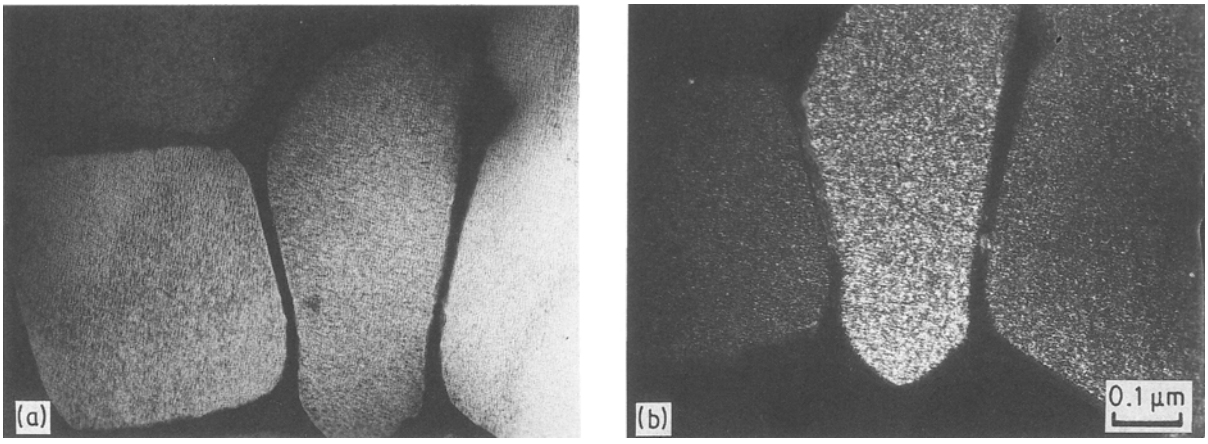

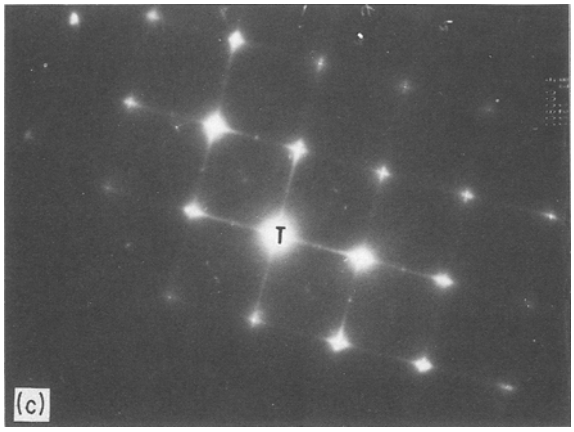

Figure 5 TEM micrographs of the cellular region in MS20, (a) BFI, (b) DFI of γ'-Ni_3Al, (c) SADP, [0 0 1] zone.

respectively. The grains in the transition regions are very irregular in size as well as shape. A particular interface morphology is dependent upon many variables, such as local temperature distribution, local solute distribution, and kinetics of the solidification process [39]. The irregularity observed in the transition region is believed to be due to the preferred solidification direction of fcc alloys, as discussed earlier.

The microstructures from the cellular solidification region are shown in Figs 5 and 6. Dark-field imaging of one of the fundamental reflections illuminates a grain containing several cells separated by low angle boundaries. This observation supports the proposed mechanism on the change of the solidification morphology as a function of ribbon thickness discussed above, in that several cells are developing from one grain. The average cell size in this region is on the order of 0.4 μm in diameter. Comparing this cell size with the one in the transition region, cell growth in a lateral direction is apparent, due to the decay of the non-preferred cells. A striated structure within the cells, indicative of spinodal decomposition [40] is shown in Fig. 5a and the corresponding selected area diffraction pattern (SADP), in Fig. 5c, exhibits satellite spots around the fundamental fcc reflections, also evidence of a spinodally decomposed structure. Also the SADP in Fig. 5c shows the superlattice reflections from the γ'-Ni_3Al phase and streaking from the fundamental reflections in $\langle 1\,0\,0 \rangle$. This streaking may

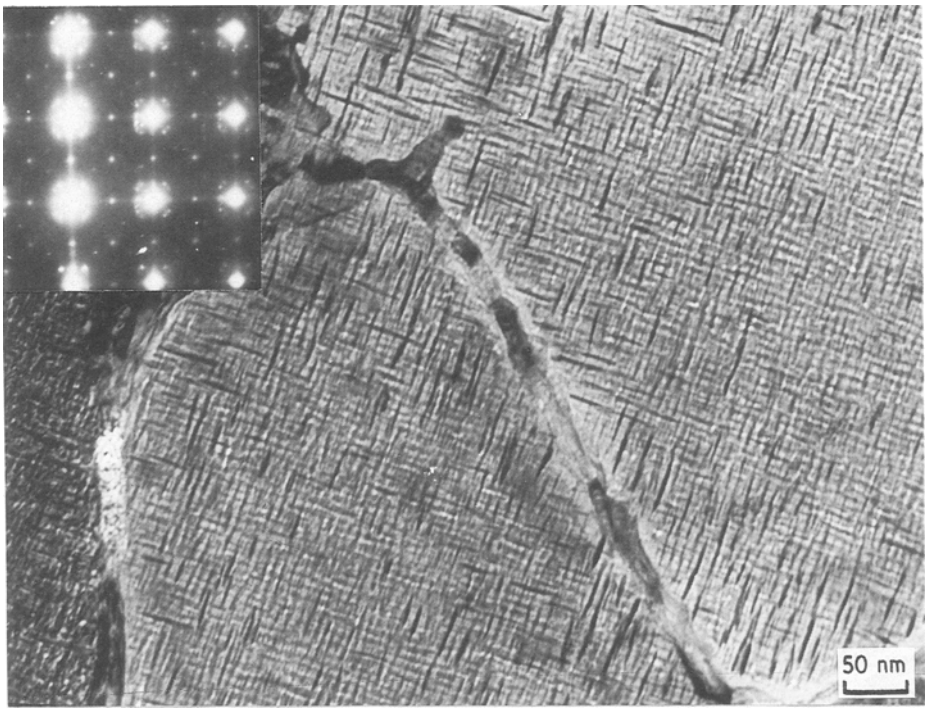

Figure 6 TEM micrograph of the cellular region in MS20 which underwent slow solid state cooling ([0 0 1] zone for the inset SADP).

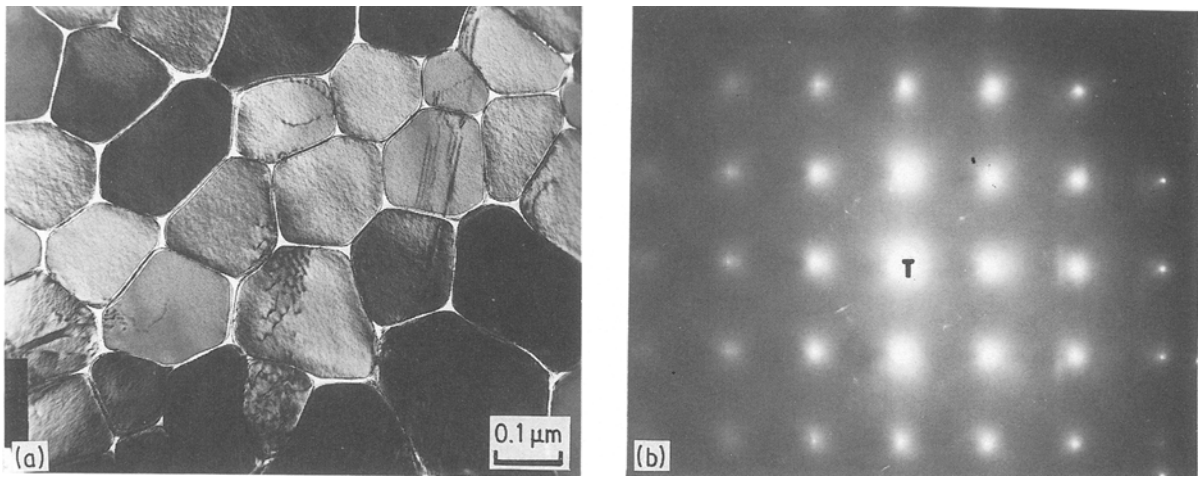

Figure 7 TEM micrographs of the cellular region in MS30, (a) BFI, (b) SADP, [0 0 1] zone, showing only γ solid solution.

be due to elastic strain associated with the fine structure from the spinodal decomposition. In addition diffuse intensity around the fundamental reflections is observed in Fig. 5c, suggesting the existence of short range order [40]. A dark-field image (DFI) of γ' from a superlattice spot in Fig. 5c is shown in Fig. 5b. The size and shape of the phase was difficult to identify because of the fine nature of the phase.

Thin foil specimens for TEM study were prepared from the different regions of the MS20 ribbon. Figure 6 shows the microstructure of the cellular solidification region of as-cast MS20. Comparing this with Fig. 5, a greater amount of transformation both at the boundaries and within the cells was observed. Within the cells the modulated structure had developed further. Also, dark thin plate-like precipitates were observed within the cells and at the cell boundaries a wall of precipitates with a thickness of about 25 nm was observed. Both phases were identified as α-Mo phase which has the Nishiyama–Wasserman orientation relationship with the matrix. A possible explanation for the different microstructures found in the cellular solidification region depending upon the ribbon taken for the examination could be that the ribbon used for Fig. 6 had undergone slower solid state cooling than the one for Fig. 5. Localized slow solid state cooling can occur from the variability in the lifting-off point from the wheel surface during the CBMS process or from the ribbon being in contact with other ribbon whilst cooling in the collection chamber. However, the average cell sizes (0.4 μm) are similar, suggesting similar solidification rates. The thickness of the plate-like α-Mo precipitate in the cells seems to be uniform (about 2 nm) and the length of the precipitate varies from approximately 20 to 50 nm. The SADP in Fig. 6 contains many diffraction spots from the various phases, γ, γ'-Ni_3Al, and α-Mo. It also has many double diffraction spots of the α-Mo phase.

The composition of the α-Mo phase at the cell boundary and that of the matrix were analysed using a scanning transmission electron microscope and the results are shown in Table III. The maximum equilibrium solubility of aluminium in the α-Mo phase is about 3 at % at 1200° C [41]. However, the solubility of aluminium in α-Mo in as-cast MS20 is about 10 at % Al presumably due to the rapid quenching. The solubility of nickel in the α-Mo phase does not show a difference in solubility from equilibrium.

3.3.2. MS30 alloy

The microstructure* of as-cast MS30 is shown in Fig. 7. No sign of transformation other than a mottled structure in the cells was observed as shown in Fig. 7a. The average cell size is on the order of 0.25 μm in diameter, suggesting a higher solidification rate for MS30 than for MS20. The solidification porosity between the cells is probably due to the high growth rate associated with the rapid solidification process. Examining the corresponding SADP, Fig. 7b, of the bright-field image (BFI) in Fig. 7a, no additional reflections other than the fundamental reflection spots were detected, confirming that all the elements had been completely solutionized. Diffuse intensity around the fundamental reflections tending to maximize in $\langle 1\,1\,0 \rangle$ was also observed. Although this could be due to thermal scattering [41], it is more likely due to the presence of short range order in the f c c matrix. Weak but sharp intensity maxima shown in Fig. 7b were not observable on the microscope screen. Since they do not have systematic regularity in the reciprocal lattice, it is not possible to identify them by indexing. They are believed to come from either specimen contamination or from adjacent grains having a similar zone axis. At any rate these intensity maxima do not represent a sign of transformation. It is interesting that $\{1\ 1/2\ 0\}$ intensity maxima which have been observed after solution treatment followed by water quenching in binary Ni–Mo alloys [42, 43] and in a ternary Ni–Al–Mo alloy [26, 17] were not observed in this alloy. This is due to the very high cooling rate obtained by the CBMS process which restricts the development of short range ordering.

Chemical analysis on the cell boundaries and on the mottled matrix in the cells was made and the results are shown in Table III. The compositional variation

*The remaining discussion involves specimens from the centre of the ribbon, unless otherwise specified.

between the two areas is not significant, meaning that homogeneous (segregationless) solidification of MS30 occurred in the centre region of the ribbon.

In summary, comparing the microstructural features of as-cast MS30 with those of as-cast MS20, a marked difference is observed, in that by applying higher wheel speed, the solidification rate is enhanced as evidenced by no transformation either at cell boundaries or in the cells, solidification porosity, no solute segregation, and smaller cell size for MS30.

3.3.3. MS30E alloy and MS30Cr alloy

The microstructures from MS30E seem to be similar to those of MS30 as shown in Fig. 8. The average cell size of MS30E is about 0.3 μm in diameter, only slightly larger than that of MS30. However, the inset SADP in Fig. 8 is different from that of MS30, Fig. 7b, in that strong reflections at the γ'-Ni_3Al superlattice positions are consistently observed in different parts of MS30E.

The alloy containing chromium, MS30Cr, shows quite different microstructures from those of the other alloys. As shown in Fig. 9a, the grains are subdivided into many cells and an unknown precipitate has formed at the cell boundaries. The cell size was difficult to measure because of the irregular shape of the grains but was estimated as about 0.4 μm diameter.

The ribbons that underwent slower solid state cooling have a different microstructure from the one shown in Fig. 9b, in that cuboidal γ' phase forms in the grains (note the superlattice spot as indicated by the arrows in the inset SADP in Fig. 9c which is missing in Fig. 9b) and a depleted zone around the precipitates at the cell boundaries and at the grain boundaries, as shown in Fig. 9c. Average size of the γ' precipitates is about 10 nm. The nature of the precipitates at both boundaries has not been determined unambiguously. The chemical compositions of the matrix and the precipitate at the cell boundaries have been determined and are given in Table III. However, the composition of the precipitate at the boundaries is not reliable because of the small size of the precipitate, about 30 nm in diameter.

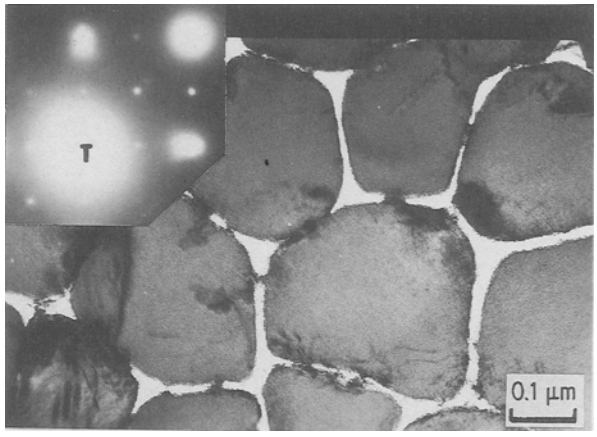

Figure 8 TEM micrograph of the cellular region in MS30E with inset [0 0 1] zone SADP.

A possible explanation for the different microstructure of the chromium-containing alloy may be that the melting temperature of the eutectic alloy is increased by approximately 30° C on addition of 10 at % Cr (see Table II). This increase in melting temperature, in turn decreases the amount of superheating of the molten metal by the same amount and this may cause solidification to start with a cellular mode rather than a planar mode. Another possible explanation could be that the addition of chromium in Ni–Al–Mo alloys increases the solidification range (i.e. larger difference between liquidus and solidus), resulting in greater constitutional supercooling. This, in turn, increases the slope of the critical gradient for planar solidification, so that solidification starts in a cellular mode rather than the planar mode. The effect of chromium

TABLE III STEM results

	Composition (at %)			
	Ni	Al	Mo	V
MS20 as-cast				
α-Mo at GB	6.6 ± 1.0	10.6 ± 0.9	80.1 ± 2.0	2.2 ± 0.1
Matrix				
as-cast	63.6 ± 0.3	24.2 ± 1.1	10.4 ± 1.4	1.7 ± 0.1
2 h/1000° C	68.3 ± 1.8	16.3 ± 1.5	13.6 ± 2.0	1.8 ± 0.2
5 h/1000° C	65.1 ± 3.0	18.4 ± 1.3	14.6 ± 3.2	1.9 ± 0.2
16 h/1000° C	67.5 ± 2.1	17.3 ± 1.9	13.6 ± 2.2	1.7 ± 0.3
50 hrs/1000° C	71.5 ± 2.5	15.0 ± 2.6	11.6 ± 0.4	2.1 ± 0.2
Matrix next to GB precipitate				
as-cast	66.6 ± 1.3	27.9 ± 0.6	3.7 ± 0.8	1.8 ± 0.3
2 h/1000° C	70.1 ± 2.0	22.8 ± 2.4	4.8 ± 0.4	2.1 ± 0.1
5 h/1000° C	72.0 ± 4.8	19.5 ± 4.0	6.4 ± 2.4	2.2 ± 0.2
16 h/1000° C	75.3 ± 2.3	20.0 ± 2.1	4.8 ± 0.3	1.8 ± 0.1
50 h/1000° C	77.7 ± 1.7	15.1 ± 2.3	4.4 ± 0.9	2.3 ± 0.2
MS30 as-cast				
Matrix	64.5 ± 1.9	16.4 ± 2.5	17.7 ± 0.6	1.4 ± 0.6
GB	64.7 ± 1.5	18.9 ± 1.4	15.3 ± 1.3	1.2 ± 0.3
MS30Cr as-cast				
Matrix	65.0 ± 2.2	16.1 ± 1.7	9.4 ± 0.5	9.4 ± 0.7
Precipitate	61.9 ± 1.9	13.8 ± 2.8	14.9 ± 1.9	9.2 ± 1.4

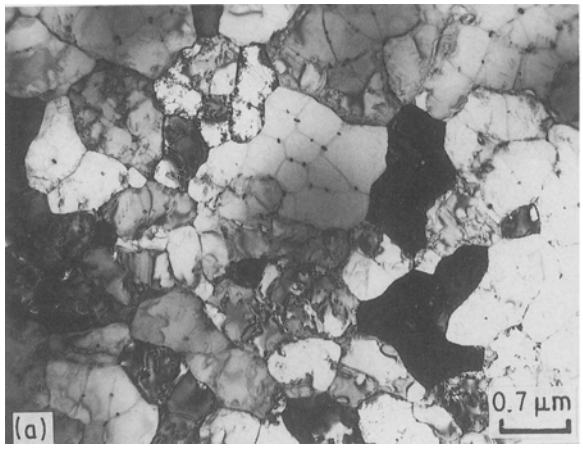

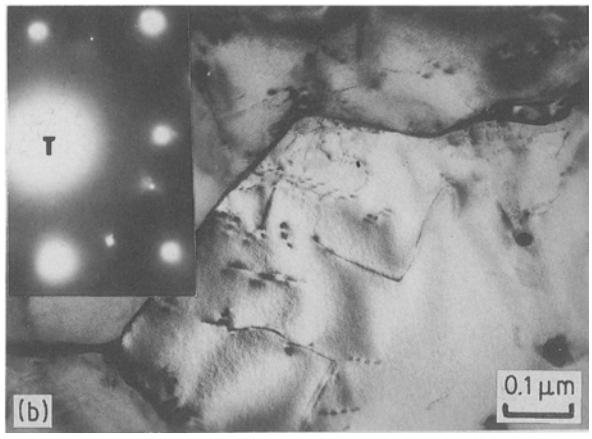

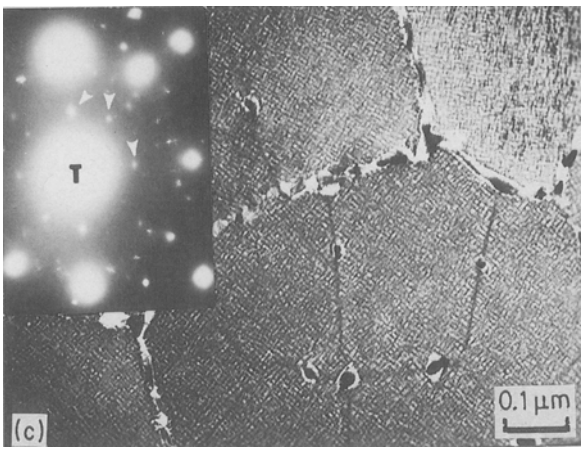

Figure 9 TEM micrographs of the cellular region in MS30Cr, (a) BFI, (b) BFI, (c) BFI of the ribbon which underwent slow solid state cooling: note the superlattice diffraction spots in the inset SADP in (c) as indicated by arrows.

addition on destabilizing the plane front growth in directional solidification mentioned in [31] supports this proposition.

3.4. Microstructure of aged MS20

The microstructure of MS20 after ageing at 1000° C for 2 h, is shown in Fig. 10a and the corresponding SADP in Fig. 10b. Large α-Mo precipitates were observed and the orientation relationship between the α-Mo phase and the matrix was determined to be;

$$(0\,1\,1)_m \| (0\,1\,1)_\alpha \text{ and } [1\,1\,0]_m \| [2\,1\,\bar{1}]_\alpha$$

by indexing the SADP as shown in Fig. 10c. This is the Nishiyama–Wassermann orientation relationship frequently observed between bcc and fcc phases. This orientation relationship between the plate-like α-Mo and the matrix has been observed in directionally solidified Ni–Al–Mo alloys [44]. It is different from that found between α-Mo fibres and the matrix formed during solidification, where the α-Mo fibres have the Bain orientation relationship with the matrix ($(0\,1\,1)_\alpha \| (0\,0\,1)_m$, $[0\,0\,1]_\alpha \| [0\,0\,1]_m$) as reported by many investigators [8, 10, 12, 25]. Close examination of the SADP in Fig. 10b revealed diffraction spots from the metastable Ni_3Mo (DO_{22}) phase but attempts to obtain the DFI of this phase were unsuccessful due to the very weak intensity.

δ-NiMo phases was observed on ageing 2 h at 1000° C as shown in Fig. 11. The δ phase can be easily distinguished from other precipitates because of its finely spaced diffraction pattern as shown in the inset SADP in Fig. 11 which is due to its complex ordered orthorhombic pseudo-tetragonal cell with unit cell dimensions of $a_0 = b_0 = 0.9108$ nm, $c_0 = 0.8852$ nm [45]. No definite crystallographic orientation relationship with the matrix has been identified. Yoshizawa *et al.* [10] have observed the δ-NiMo phase in directionally solidified Ni–Al–Mo alloys on ageing at 1000° C after solutionizing at 1260° C followed by ice water quenching. However, in that work the δ phase was not observed until after ageing for 100 h at 1000° C because a thin wall of γ′ phase formed around α during quenching was still present, delaying the pseudo-peritectoid reaction ($\gamma + \alpha \rightarrow \gamma' + \delta$). The early formation of δ phase in this work is because the diffusion distance to form δ phase is much reduced and there is no γ′ surrounding the α phase. The δ phase exhibits a faulted structure as shown in Fig. 11.

After ageing for 5 h at 1000° C, the metastable DO_{22} spots still exist. The BFI shown in Fig. 12a shows the δ phase present at the boundaries and a precipitate-free zone next to the δ phase. The inset SADP is from the δ phase marked X in Fig. 12. After ageing 16 h at 1000° C, the metastable DO_{22} reflection disappears, as shown in Fig. 13.

STEM analysis was made on the matrix between the α plates and on the precipitate-free region next to the δ phase at the boundaries as a function of ageing time at 1000° C. The results are summarized in Table III. The precipitate-free region contains consistently less molybdenum and slightly more aluminium than the matrix between the α plates. This suggests that the precipitate-free region is γ′ and the matrix between the α is γ, in accord with the reported pseudo-peritectoid reaction ($\gamma + \alpha \rightarrow \gamma' + \delta$).

4. Summary and conclusions

1. The melting temperature and the γ′ solvus of the MS30 alloy are 1302 and 1245.5° C, respectively. The heat of fusion of the MS30 alloy was measured to be $8.92 \pm 0.45\,kJ\,mol^{-1}$. The melting temperature of MS30E and MS30Cr were measured to be 1290 and 1320° C, respectively.

2. The thickness of ribbon produced by the CBMS

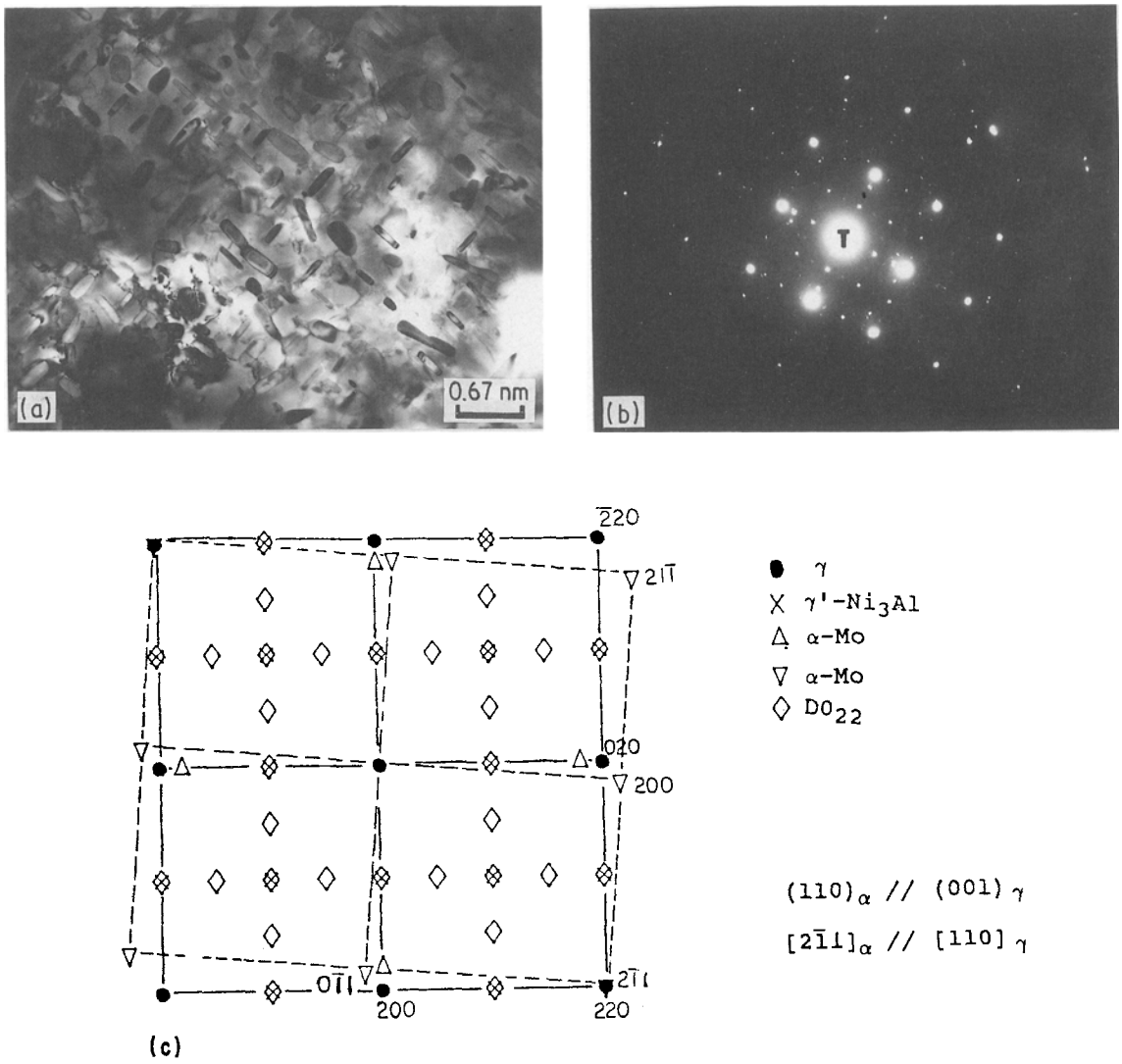

Figure 10 TEM micrographs of MS20 after ageing for 2 h at 1000° C, (a) BFI, (b) SADP, [0 0 1] zone, (c) indexed SADP in (b).

process increases as the wheel speed decreases whilst the ribbon width is independent of the wheel speed and alloy composition. The ribbons, except MS30Cr alloy, have a solidification mode that changes from planar to cellular to dendritic, on going from the wheel side to free side of the ribbon. MS30Cr alloy showed only cellular solidification mode throughout the ribbon thickness.

3. The solid state cooling must be considered one of the important processing parameters since the microstructure of the ribbon varies greatly depending upon the solid state cooling after solidification, even within a given batch of material.

4. Using a high wheel speed, complete solutionization of alloying elements in the MS30 alloy was possible through CBMS process. However, the MS30E and MS30Cr alloys showed some sign of transformation at the cell boundaries, indicating that

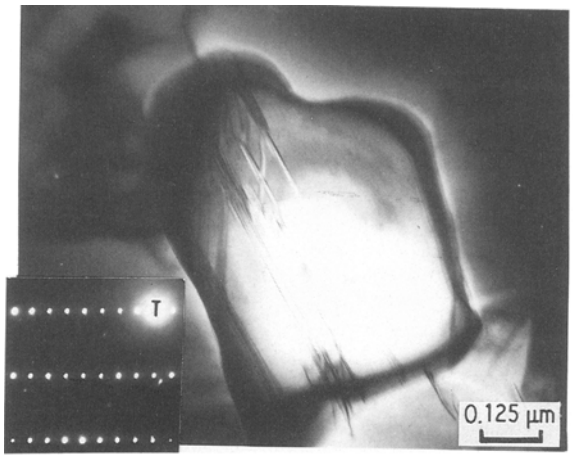

Figure 11 BFI of δ-NiMo after ageing for 2 h at 1000° C.

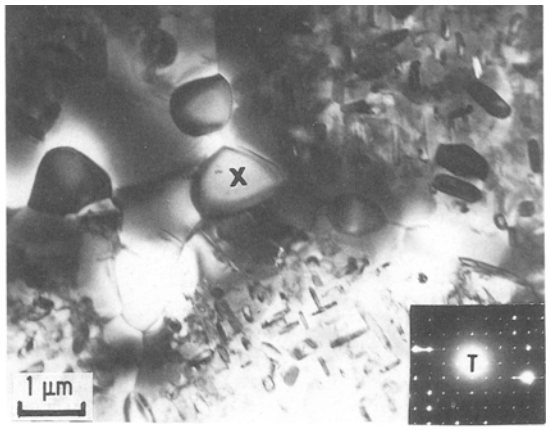

Figure 12 TEM micrograph of MS20 after ageing for 5 h at 1000° C with inset [0 0 1] zone SADP.

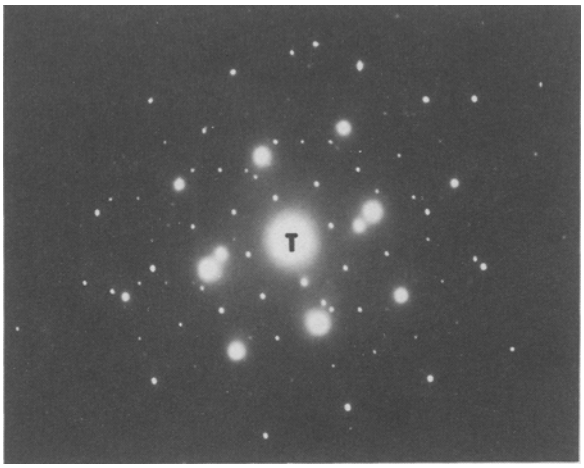

Figure 13 Electron diffraction pattern after ageing for 50 h at 1000° C, [0 0 1] zone.

an even higher wheel speed is necessary for complete solutionization of these alloys.

5. The embrittling intermetallic δ-NiMo phase was observed after ageing for only 2 h at 1000° C probably due to the more homogeneous distribution of the second phases in this rapidly solidified material than in solution-treated directionally solidified Ni–Al–Mo alloys.

Acknowledgements

This paper is based on work by S. Y. L. in partial fulfilment of the requirements for the PhD degree at Illinois Institute of Technology. The help from NASA Lewis Research Center on material preparation is greatly appreciated. The authors also thank Nestor Zaluzec and Russ Cook at Argonne National Laboratory for provision of TEM facilities, and Ricardo Schwarz at Los Alamos National Laboratory for use of DTA. S. Y. L. would like to thank the Department of Metallurgical and Materials Engineering at I. I. T. for financial support.

References

1. M. COHEN and M. FLEMINGS, Proceedings on Rapidly Solidified Crystalline Alloys, Morristown, May 1985, edited by S. Das, B. Kear and C. Adam (TMS, Warrendale, 1985) p. 3.
2. P. DUWEZ, R. WILLENS and W. KLEMENT Jr, *J. Appl. Phys.* **31** (1960) 1136.
3. P. DUWEZ and R. WILLENS, *Trans. AIME* **227** (1963) 362.
4. W. KLEMENT Jr, R. WILLENS and P. DUWEZ, *Nature* **187** (1960) 869.
5. R. JECH, T. GLASGOW, N. ORTH and T. MOORE, *J. Met.* April (1984) 41.
6. S. SAVAGE and F. FROES, *ibid.* April (1984) 20.
7. T. ISHII, D. DIQUETTE and N. STOLOFF, *Acta Metall.* **29** (8) (1981) 1467.
8. H. SPRENGER, H. RICHTER, J. NICKL, *J. Mater. Sci.* **11** (1976) 2075.
9. F. LEMKEY, Proceedings of the 3rd International Symposium on Superalloys: Metallurgy and Manufacture, edited by B. Kear, D. Muzyka, J. Tien and S. Wlodek (Claitor's Publishing Division, Baton Rouge, 1976) p. 321.
10. H. YOSHIZAWA, K. WAKASHIMA, S. UMEKAWA and T. SUZUKI, *Scripta Met.* **15** (1981) 1091.
11. F. D. LEMKEY, NASC-76115-30, Final Report on Navair Contract N62269-75-C-0129 (United Technology Research Center, Hartford, 1975).
12. M. HENRY, *Scripta Met.* **10** (1976) 955.
13. J. M. TARTAGLIA and N. S. STOLOFF, *Met. Trans.* **12A** (1981) 1891.
14. Y. G. NAKAGAWA, A. OHOTOMO and Y. SAIGA, Proceedings 4th International Symposium on Superalloys, Champion, September 1980, edited by J. Tien, S. T. Wlodek, H. Morrow III, M. Gell and G. E. Maurer (ASM, Metals Park, 1980) p. 267.
15. H. YOSHIZAWA, K. WAKASHIMA and S. UMEKAWA, *J. Mater. Sci.* **17** (1982) 3484.
16. D. SNOW, E. BRENIAN and B. H. KEAR, Proceedings 4th International Symposium on Superalloys, Champion, September 1980, edited by J. Tien, S. T. Wlodek, H. Morrow III, M. Gell and G. E. Maurer (ASM, Metals Park, 1980) p. 189.
17. J. C. WILLIAMS and P. L. MARTIN, *Met. Trans.* **16A** (1985) 1983.
18. M. TWIGG, A. J. MELMED, R. KLEIN, M. J. KAUFMAN and H. L. FRASER, Proceedings 5th International Symposium on Superalloys, Champion, September 1984, edited by M. Gell, C. S. Kortovich, R. H. Bricknell, W. B. Kent and J. F. Radavich (TMS-AIME, Warrendale, 1984) 631.
19. A. E. ANDERSON, A. R. COX, T. D. TILLMAN and E. C. VAN REUTH, Proceedings 2nd Conference on Rapid Solidification Processing Principles and Technologies III, Reston, November, 1980. edited by R. Mehrabian, M. Cohen and B. H. Kear (Claitor's Publishing Division, Baton Rouge, 1980) p. 416.
20. P. MARTIN and J. WILLIAMS, Proceedings International Conference on Solid-Solid Phase Transformations, Pittsburgh, August, 1981, edited by H. Aaronson, D. Laughlin, R. Sekerka and C. Wayman (TMS-AIME, Warrendale, 1982) p. 757.
21. P. MARTIN, H. LIPSITT and J. WILLIAMS, Proceedings Conference on Rapid Solidification Processing Principles and Technologies, Reston, November, 1977, edited by R. Mehrabian, M. Cohen, and B. H. Kear (Claitor's Publishing Division, Baton Rouge, 1978) p. 123.
22. E. AIGELTINGER, S. BATES, R. GOULD, J. HREN and F. RHINES, *ibid.* p. 291.
23. D. SNOW, MRS Symposium Proceedings on Rapidly Solidified Amorphous and Crystalline Alloys, Boston, November, 1981, edited by B. Kear and B. Giessen (Elsevier North-Holland, New York, 1982) p. 523.
24. H. GRAY, NASA TM 73714 (1971).
25. M. NEMOTO, T. HONDA, Y. NAKAGAWA, Y. SAIGA and H. SUTO, *Trans. Jpn Inst. Met.* **21**(8) (1980) 495.
26. K. WAKASHIMA, K. HIGUCHI, T. SUZUKI and S. UMEKAWA, *Acta Met.* **31** (11) (1983) 1937.
27. D. MIRACLE, K. LARK, V. SRINIVASAN and H. LIPSITT, *Met. Trans.* **15A** (1984) 481.
28. S. Y. LEE and P. NASH, *Acta Metall.* (1989) submitted.
29. S. Y. LEE, PhD thesis, I.I.T., Chicago, 1988.
30. M. CHASE, *Bull. Alloy Phase Diagrams.* **4**(1) (1983) 124.
31. D. D. PEARSON and F. D. LEMKEY, Metal Society Conference on Solidification and Casting of Metals (The Metal Society, Sheffield, 1979) p. 526.
32. S. C. HUANG and A. M. RITTER, Proceedings of Symposium on Chemistry and Physics of Rapidly Solidified Materials, St Louis, October, 1982 (TMS-AIME, Warrendale, 1983) p. 25.
33. S. C. HUANG, R. P. LAFORCE, A. M. RITTER and R. P. GOEHNER, *Met. Trans.* **16A** (1985) 1773.
34. S. N. TEWARI and T. K. GLASGOW, *ibid.* **18A** (1987) 1663.
35. H. DAVIES, N. SHOHOJI and D. WARRINGTON, Proceedings 2nd Conference on Rapid Solidification Processing Principles and Technologies III, Reston, November, 1980. edited by R. Mehrabian, M. Cohen and B. H. Kear (Claitor's Publishing Division, Baton Rouge, 1980) p. 153.
36. P. NASH and T. GLASGOW, *Acta Met.* **35** (11) (1987) 2627.

37. E. L. HALL and S. C. HUANG, *Met. Trans.* **17A** (1986) 407.
38. M. COHEN, B. KEAR and R. MEHRABIAN, *ibid.* 1.
39. W. TILLER, "Physical Metallurgy" 2nd edn, edited by R. Cahn, (North-Holland, Amsterdam, 1970) p. 422.
40. J. W. EDINGTON, "Practical Electron Microscopy in Materials Science" (Van Nostrand Reinhold, New York, 1976) p. 88–105.
41. S. Y. LEE, K. J. LEE and P. NASH, *Bull. Alloy Phase Diagrams* in press.
42. K. VASUDEVAN and E. STANSBURY, MRS Proceedings on Materials Problem Solving with the Transmission Electron Microscope (MRS, Pittsburgh, 62, 1986) p. 337.
43. P. MARTIN and J. WILLIAMS, *Acta Met.* **32** (10) (1984) 1681.
44. N. NEMOTO, T. HONDA, Y. NAKAGAWA, Y. SAIGA and H. SUTO, *Trans. J. Inst. Met.* **21** (8) (1980) 505.
45. C. SHOEMAKER and D. SHOEMAKER, *Acta Cryst.* **16** (1963) 997.

Received 11 November 1988
and accepted 26 April 1989